Fundamental photophysics and optical loss processes in Si-nanocrystal-doped microdisk resonators

Rohan D. Kekatpure[*] and Mark L. Brongersma[†]

Geballe Laboratory of Advanced Materials, Stanford University, Stanford, California 94305, USA

We report a detailed analytical, numerical, and experimental study of microdisk resonators doped with nanometer sized silicon quantum dots (nanocrystals). An intuitive analytical ray-optics-based model is developed and used to capture the behavior of the quality factor (Q) as a function of the disk size and the attenuation coefficient. Two regimes in the behavior of Q with the disk size establish a simple design rule for optimizing the performance of these cavities. The validity of our analytical model is verified by full-vectorial finite element method calculations of the microcavity modes. Based on the predictions of the analytical and numerical calculations, we have fabricated microdisk resonators with diameters ranging between 2 and 8 μm. $Q > 10^3$ are obtained for disk radii as small as 4 μm—highest observed for Si-nanocrystal-doped microdisk resonators. The fundamental limit on Q is estimated by quantifying all of the potential optical loss processes through a careful analysis which includes the effects of nanocrystal size distribution. Our theoretical calculations match well with experiments and reveal that the line-edge roughness scattering and radiation loss can be minimized sufficiently to enable study and quantification of more fundamental optical loss processes of this material due to band-to-band absorption, Mie scattering, and free-carrier absorption in the Si nanocrystals. Using the experimental Q's and the mode volumes, we predict the maximum low-temperature Purcell enhancement factor in our structures on the order of 6 and with some design improvements enhancements up to 50 can be realized.

I. INTRODUCTION

Photophysics studies on silicon nanocrystals (nc-Si) have been of interest for two reasons: First, they have a potential to provide us with low cost, Si-based incoherent and coherent light sources [1–4]. Second, such studies have led to new insights into the fundamental optical properties of confined indirect band-gap semiconductors [5–15] and the prominent role of interfaces between glassy and crystalline materials [8,16]. Recently, nc-Si has also been considered as a broadband sensitizer for pumping of rare earth ions emitting at 1.55 μm wavelength [17–21].

Study of photoluminescence (PL) from nc-Si is approached from either a materials-physics or a device-physics point of view. The materials-physics approach concentrates on the issues of formation and evolution of nanocrystals [22–25], origin and the mechanism of PL [5,7–9,11,12,14,26], and radiative and/or nonradiative processes taking place inside nc-Si and its surface. With the notable exception of the single nanostructure studies of Sychugov *et al.* [27,28], investigations of this type utilize silicon-rich oxide (SRO) films in various experimental configurations (varying temperature, optical excitation, magnetic field, etc.). The device-physics approach inquires about the possibility of achieving net gain from a nc-Si material system. Typically, planar or ridge and/or rib waveguides are used for such studies [1,29–31].

In a hybrid approach, more complex structures are used to probe materials- and device-physics simultaneously. The structures in such studies should be able to controllably modify the interaction of the emitter with its surrounding environment. Optical resonators (cavities) achieve such a modification of the emitter-environment interaction in a dielectric environment. The efficacy of a resonator in bringing about a change in an emitter's local electromagnetic environment is measured in terms of its quality factor, Q, and modal volume, V_m, or, equivalently, in terms of the ratio Q/V_m [32,33]. Because of their versatility and potential applications, much recent literature has been devoted to the optimization of resonators in various geometries and material systems [34–37]. Among these, azimuthally symmetric resonator structures such as microring, microdisk, microtoroid, and microspheres are particularly interesting owing to a relative ease in their fabrication, measurements, and analysis. As a result, they have been effectively used for fundamental studies as well as demonstration of lasing devices in atomic and semiconductor material systems [36–49]. These resonators are thus ideal structures for exploring the optical properties of silicon nanocrystals.

Azimuthally symmetric resonators in Si, SiO$_2$ and III-V semiconductor systems are particularly well studied and $Q > 10^6$ in the near-infrared (NIR) wavelength range (1000–1550 nm) have been routinely demonstrated [44,46,49,50]. The Q limiting processes in these resonators have been analyzed in detail and are quite well understood [36,37,43,50]. In contrast, the Q of microdisk resonators containing nc-Si are seen to be limited to values $<10^3$ in the visible-NIR wavelength range (600–900 nm) [51]. In spite of its fundamental and technological significance, there exists no detailed study of the Q-limiting fundamental optical loss processes in microdisk resonators containing Si quantum dots (QDs).

*rohank@stanford.edu

†brongersma@stanford.edu

The characteristics of the microdisk resonators containing Si QDs in the visible-NIR wavelength range differ in several aspects from those of the similar devices fabricated in the III-V, Si and SiO$_2$ systems. High-index-contrast systems such as III-V semiconductors and silicon lend themselves naturally to the fabrication of microdisks with diameter $D \sim 2$ μm. On the other hand, reduction of the resonator sizes in low-index systems is difficult because of weak field confinement. High-Q azimuthally symmetric resonators in these systems therefore have diameters on the order of 100 μm [37,46]. These resonators are typically coupled to atomic emitters (e.g., Er^{3+}) for demonstrations of lasing and quantum electrodynamics experiments [46]. Because of the small absorption cross section of atomic emitters (e.g., $\sim 10^{-21}$ cm^2 for Er^{3+}) high Q of these resonators is maintained even upon doping with such atoms. The SRO material system combines semiconductor (Si) quantum dots with a low-index dielectric host SiO$_2$, which prevents a reduction of mode volume because of the radiation loss. The absorption cross section of Si QDs at visible-NIR wavelengths is [52] $\sim 10^{-18}$ cm^2 which, for a microdisk fully filled with Si nanocrystals, ultimately limits the Q to $\sim 10^4$. Any attempt to reduce the QD concentration comes at a cost of reduction in the refractive index of the material and, thus, an increase in the radiation loss.

Additionally, there are several factors which, although present at longer wavelengths (~ 1.55 μm), are not significant in the cavity design at those wavelengths. The same factors become quite significant at shorter wavelengths (600–900 nm) and make it a challenging task to achieve high Q/V_m figures for nc-Si containing SRO microdisks at these wavelengths: (1) there is a loss contribution resulting from band-to-band absorption in the nanocrystals, which becomes significant for energies above nc-Si band gap, (2) Mie scattering from the dense nanocrystal ensemble plays a much more important role in the visible-NIR wavelengths owing to an inverse fourth-power wavelength dependence, (3) the refractive index contrast of air to SRO (refractive index ~ 1.7) is much less compared to Si or GaAs (refractive index ~ 3.5); this results in a significant radiation loss for micronsized resonators making their size reduction difficult, and (4) the sidewall scattering losses are much more significant in the visible-NIR wavelength compared to those at 1.55 μm. Inclusion of the effects of the QD size distribution is crucial in order to accurately model these various loss mechanisms.

It is the aim of the present work to carry out a theoretical and experimental investigation of the Q-limiting processes in microdisk resonators containing silicon nanocrystals in the visible-NIR wavelength range by appropriately accounting for the effects of the Si QD size distribution. The organization of the paper is as follows: Section III (following a brief description of SRO optical constants in Sec. II) provides an intuitive ray-optics-based model of a generic microdisk resonator. This is used to predict the size dependence of quality factors and, with the knowledge of the total loss coefficient, to provide a range of sizes for optimizing the Q and the Q/V_m figures of merit. Section IV is devoted to a fullvectorial finite element method (FEM) calculation of microdisk resonator modes. FEM simulations make it possible to calculate the microdisk modes with realistic sidewall profiles, yielding the radiation profiles for optimizing collection optics, and providing a way to calculate the Q and mode volume. A comparison between the FEM simulations and the ray-optics model also highlights the domain of applicability of the latter for the material system in our experiments. Experimental results pertaining to fabrication and optical characterization of microdisk resonators are presented in Sec. V. Size-dependent quality factors from fabricated microdisks are compared with predictions from FEM and ray-optics models in Sec. VI. In Sec. VII we consider various loss mechanisms limiting the performance of our fabricated microdisks. Finally, in Sec. VIII we assess our experimental structures for their potential in bringing about spontaneous emission enhancement in silicon nanocrytals. We also discuss the implication of the present work for achieving stimulated emission in nc-Si.

II. DEPOSITION AND OPTICAL CHARACTERIZATION OF SRO THIN FILMS

Design and analysis of patterned dielectric resonator structures requires knowledge of the optical properties of the unpatterned material. This brief section is therefore devoted to the presentation of the optical constants of the SRO films utilized in our studies. These films were prepared by plasma enhanced chemical vapor deposition (PECVD) using 2% silane (SiH$_4$) (diluted in N$_2$) and nitrous oxide (N$_2$O) as precursor gases on a $\langle 100 \rangle$-oriented silicon substrate with a p-type doping density of 4.5×10^{15} cm^{-3}. The deposition temperature and pressure were 350 °C and 650 mTorr, respectively. The SiH$_4$:N$_2$O flow ratio was varied to alter the silicon concentration (and to indirectly control the nc-Si size). Finally the films were annealed at 1100 °C to form the nanocrystals. The post-anneal thickness of the nc-Si films was 330 nm as measured by ellipsometry and cross-sectional scanning electron microscopy (SEM). Identical films were deposited on 450-μm-thick fused silica substrates to be used for light transmission measurements. Nanocrystal synthesis procedure reported above is one of the standard methods for the preparation of optically active nc-Si thin films. The detailed materials characterization of nc-Si formed by this procedure is reported in literature [22,24,25]. The materials characterization of films prepared in our study appear elsewhere [53,54].

The complex refractive index ($\tilde{n}$) is defined as $\tilde{n} = n + ik$. In the subsequent sections, we adopt a convention where the time variation of the electromagnetic fields (at an angular frequency ω) is assumed to be $\sim e^{-i\omega t}$. Therefore, $k > 0$ represents an optical loss. Real and imaginary parts of the refractive index of the unpatterned SRO films in our study were obtained from spectroscopic ellipsometry and transmission measurements, respectively. The transmission measurements were performed on the SRO films deposited on fused silica substrates. Ellipsometry analysis was carried out using the Woollam M2000 spectroscopic ellipsometer to obtain the real part of the refractive index as a function of wavelength. The same instrument was used for obtaining light transmission data in order to extract the absorption coefficient and the imaginary part of the refractive index. Analysis of the ellipsometric data was performed by Woollam's WVASE soft-
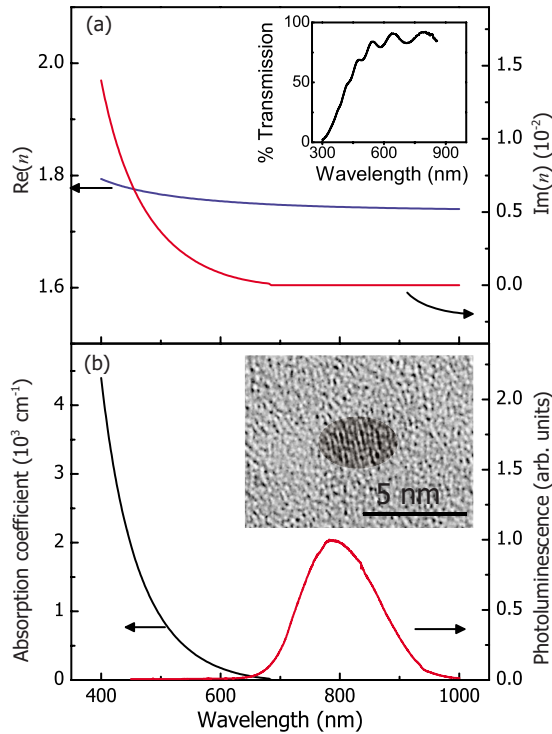
FIG. 1. (Color online) (a) The optical constants (real and imaginary refractive indices) of the annealed SRO thin films determined by ellipsometry and the Swanepoel methods. Shown in the inset is the transmission spectrum of a 1-μm-thick SRO film used in the Swanepoel method calculation. (b) The absorption coefficient and the typical photoluminescence spectrum of an unpatterned SRO film used in this work. The $\langle 111 \rangle$ lattice fringes from a Si nanocrystal are visible against an amorphous background shown in the inset. The crystalline region is highlighted in a dark tone for clarity.

ware and the transmission data were analyzed by Swanepoel's method [55]. Figure 1(a) shows the wavelength-dependent real and imaginary parts of the refractive index. Figure 1(b) shows the absorption coefficient (obtained from the imaginary part of the refractive index) and the PL from an annealed SRO film. The presence of nanocrystals in SRO was confirmed by high resolution transmission electron microscopy (HR-TEM), which reveals the Si nanocrystals as lattice fringes over an amorphous background as shown in the inset of Fig. 1(b). The measured lattice fringe spacing of 0.31 nm is consistent with $\langle 111 \rangle$ planes of Si. The results shown in Fig. 1 are very similar to the ones reported in previous works [56].

Measurements of the optical constants presented in this section are subsequently used in the analytical and numerical calculations presented hereafter. This section also provides useful information about the material loss in nc-Si, which dictates the upper limit on the Q achievable in this system at various wavelengths.

III. SIZE-DEPENDENT QUALITY FACTOR OF MICRODISKS FROM RAY-OPTICS MODEL

Azimuthally symmetric structures such as microdisks support resonant modes which are confined inside the disk by
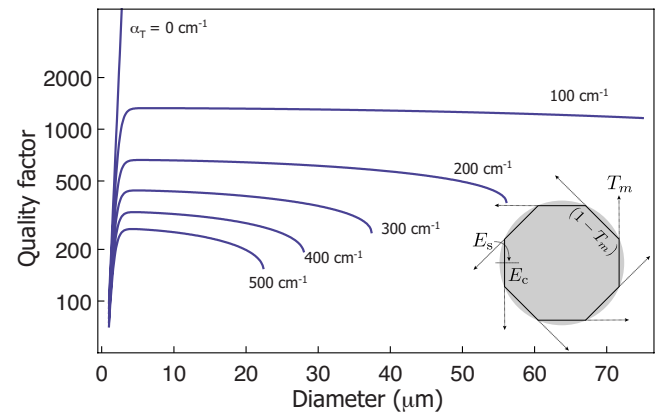

FIG. 2. (Color online) Quality factor versus microdisk diameter calculated using the ray-optics model on log-linear axes. Quality factor is calculated using Eq. (4) for 0 cm^{-1} < α_T < 500 cm^{-1} at a wavelength of 750 nm. The dependence of Q shows exponential and saturated regimes consistent with the simplified equations (5) and (6). The effective index for the calculation is set to $n_{eff} = 1.56$ and is obtained by solving the infinite slab waveguide equation [60] whereas the loss values for the different curves are shown next to them. The inset shows the schematic used for derivation of the analytical formula for Q [Eq. (4)].

multiple total internal reflections from its circumference. The electromagnetic field of these modes circulates along the disk periphery and, as a result, these modes are known as whispering gallery modes (WGMs) [57,58]. A WGM is characterized by the number of nodes it possesses along the radial ($\hat{r}$), azimuthal ($\hat{\phi}$), and axial ($\hat{z}$) directions. Typically, higher order radial and axial modes are either very lossy or difficult to excite controllably. Most of the discussion about microdisk modes therefore pertains to the fundamental axial and radial modes with varying azimuthal mode numbers. Consequently, WGMs are mostly addressed just by their azimuthal mode number with the implicit assumption of their fundamental order in the other two directions.

In this section we use a ray-optics-based model of a fundamental microdisk mode to develop an analytical expression for its total quality factor, Q_{total}. Although numerical solutions of field equations result in more accurate predictions for specific structures, this accuracy comes at the cost of increased time. The advantage of the ray-optics picture therefore lies in predicting trends and establishing intuitive and general design rules. This model also helps in quantifying the two size-dependent operational regimes of microdisk resonators. Identification of these regimes have important implications for optimization of the Q and Q/V_m figure of merit for cavities fabricated in low-index-contrast systems such as SRO.

In the ray-optics model, a steady state, resonant WGM is approximated by a light ray traveling along the microdisk periphery at a grazing incidence as depicted in Fig. 2 (inset). The mode is sourced by the electric field, E_s, of an emitting quantum dot. On each bounce of the ray on the periphery, part of the energy leaks out and the remainder is reflected. The "per-bounce transmission coefficient" for the mth order azimuthal mode, T_m, is given as [59],

$$T_m = \exp\left(-\frac{2}{3} s_{m,1} \cos^3 \theta_c\right). \quad (1)$$

In Eq. (1), $s_{m,1}$ is the first zero of the mth-order Bessel function and θ_c is the critical angle of incidence at the disk-air boundary, obtained in terms of the effective index (n_{eff}) of the microdisk as $n_{\text{eff}} \sin(\theta_c) = 1$. For a resonant mode, the circulating intensity is obtained by following the propagation of the field inside the cavity and imposing a self-consistency condition on the cavity field (E_c) after one round trip. This yields the source-normalized cavity intensity as

$$I_c = \left|\frac{E_c}{E_s}\right|^2 = \frac{1}{|1 - (1 - T_m)^m e^{i2m\psi_m} e^{i\beta_m L_m} e^{-\alpha_T L_m/2}|^2}. \quad (2)$$

Here ψ_m is the phase change upon reflection back into the disk, λ_m is the free-space resonant wavelength, $\beta_m = 2\pi n_{\text{eff}}/\lambda_m$ is the propagation constant of the mode in the $+\hat{\phi}$ direction, α_T is the total power attenuation coefficient for the mode, and L_m is the polygonal round trip path length, given by

$$L_m = \pi D \frac{\sin(\pi/2m)}{\pi/2m}. \quad (3)$$

The factor of $2m$ in Eq. (3) results from the fact that the Poynting vector of a given azimuthal mode m experiences $2m$ symmetrical mirror reflections along the microdisk periphery [59]. The full width at half-maximum (FWHM) of the mth azimuthal resonance ($\Delta\lambda_m = \lambda_{m+} - \lambda_{m-}$) is obtained by solving Eq. (2) for the values of free-space wavelengths ($\lambda_{m\pm}$) at which the circulating intensity I_c drops to one-half of its maximum value. The total quality factor of the mth-order mode is thus given by

$$Q_{\text{total}} \equiv \frac{\lambda_m}{\Delta\lambda_m} = \frac{\pi n_{\text{eff}} L_m}{2\lambda_m} \frac{1}{\sin^{-1}\left[\sinh\left(\dfrac{\alpha_T L_m + 2\mu_m}{4}\right)\right]}, \quad (4)$$

where $\mu_m = -m \ln(1 - T_m)$ is the measure of power leaking out of the cavity. $\mu_m \to 0$ with increasing disk diameter or increasing index contrast.

The size-dependent Q of microdisk modes predicted by Eq. (4) is depicted in Fig. 2. Initially, the quality factor increases with increasing disk diameter. Upon further increasing the size, Q almost saturates to a steady value which depends on the total propagation loss α_T in the structure. These trends in Q can be explained in a straightforward manner once Eq. (4) is cast into more familiar forms for some limiting cases. For low attenuation, small disk size, or low refractive index, $\alpha_T L_m \ll \mu_m \ll 1$ and the corresponding Q in this "radiation-limited" regime is given by

$$Q_{\text{rad}} \simeq \frac{\pi n_{\text{eff}} L_m}{\mu_m \lambda_m} \simeq \frac{\pi n_{\text{eff}} L_m}{m \lambda_m} \exp\left(\frac{2}{3} s_{m,1} \cos^3 \theta_c\right). \quad (5)$$

For high attenuation or high core index, $\mu_m \ll \alpha_T L_m \ll 1$. The Q in this "loss-limited" regime simplifies to

$$Q_{\text{loss}} \simeq \frac{2\pi n_{\text{eff}}}{\alpha_T \lambda_m}. \quad (6)$$

Equation (5) implies that for (a) low attenuation, or (b) sufficiently small size, or (c) low core index, the Q factors are limited by radiation loss. In this regime, the increase in Q with disk diameter is (approximately) exponential. As the disk size increases (or equivalently if the loss is high), the radiation out of the disk no longer limits the Q and it enters the "loss-limited" regime. In this regime, as implied by Eq. (6), Q no longer varies with the disk size. Upon further increasing the disk size, Eq. (4) predicts that Q slowly decreases with increasing disk size. Mathematically, this can be seen as a consequence of the breakdown of $\sin^{-1} x \sim x$ and $\sinh x \sim x$ approximations as $\alpha_T L_m \to 1$. The decreasing trend in Fig. 2 can be obtained by expansions of $\sin^{-1}(x)$ and $\sinh(x)$ functions in Eq. (4) beyond the first order. Physically, $\alpha_T L_m \to 1$ means that, because of the high attenuation inside the disk core, the electromagnetic mode travels less than one complete round trip. As a result, no traveling or standing wave pattern can be sustained inside the resonator in the steady state and the Q is degraded. For most low-loss dielectric systems, the dimensions required to reach the "round-trip" limited regime are many orders of magnitudes higher than the typically used sizes [37].

The behavior predicted by Eq. (4) and plotted in Fig. 2 leads to a direct prescription for optimization of the Q/V_m figure for SRO microdisk resonators. Following an initial exponential increase, Q saturates to a steady (loss-dependent) value with increasing disk diameter. To first order, the mode volume tracks the disk diameter linearly. The maximum in Q/V_m for these resonators can thus be expected at a size which is just outside the radiation-limited regime. This size is obtained at a disk diameter which equates Q_{rad} to Q_{loss}.

The ray-optics model described by Eqs. (4)–(6) correctly captures the trends in the Q factor observed in most dielectric systems. However, there are important differences in high- and low-index systems when it comes to the accuracy of the actual numbers predicted. For high-index systems such as Si or GaAs, light is confined very tightly inside the core of the disk, such that even for diameters as small as 2 μm, the azimuthal mode number, m, tends to be high. The Q of these disks is thus limited by the power attenuation inside the disk core for most physically realizable disk diameters. The ray-optics picture therefore yields accurate values of Q even for small sized disks. However, validity of the ray-optics model breaks down for small values of azimuthal mode number m as is the case for low-index systems such as SRO. The actual values of Q predicted by Eq. (4) in the radiation-limited regime agree only within an order of magnitude with rigorous numerical calculations. The comparison of the ray-optics model with numerical simulations and experiments in Sec. VI will further highlight its range of applicability.

IV. FEM CALCULATION OF MICRODISK WHISPERING GALLERY MODES

The ray-optics model yields analytical results that display good qualitative agreement with experimental trends. How-

ever, there are several design and measurement details that require a precise calculation of fields inside the resonator structure. For instance, numerical field calculations are required for (1) knowledge of the radiation pattern of the resonant WGM and optimization of free-space collection optics, (2) calculation of modal volume of a specific WGM, (3) estimating the optimal pedestal dimensions (wider pedestals cause leakage of whispering gallery mode into high-index Si whereas too thin pedestals compromise the structural integrity of the devices), and (4) accurate calculation of the Q_{rad} for small, low-index resonators.

Several authors have considered numerical calculations of microdisk WGMs by various methods [49,58,61]. In such simulations, there is a well-known trade-off between accuracy, dimensionality, memory resources, and speed. Three-dimensional simulations are full vectorial, but they are prohibitively costly in terms of memory and speed, whereas two-dimensional simulations require *a priori* classification of modes based on their polarization [46]. Microdisk resonators can have slanted sidewalls depending on the etching conditions and such a classification may not always be possible. Thus a full-vectorial calculation is desired. Fortunately, because of the azimuthal symmetry of the structure, all the resonant fields can be assumed to have an $e^{-im\phi}$ dependence with an integer value of m. The independent cylindrical coordinates in the problem therefore reduce to r and z. This reduction of dimensionality from 3D to 2D makes it possible to accurately calculate the microdisk modes without imposing any simplifying assumptions on their polarization. Several recent examples of such "full-vectorial 2D" calculations are found in the literature [37,49,61]. However, we will briefly outline the simulation methodology that we have used in this paper.

The starting point for our calculations is the vector wave equation written in terms of the magnetic field,

$$\nabla \times (\boldsymbol{\epsilon}_r^{-1} \nabla \times \mathbf{H}) = k_0^2 \mathbf{H}, \tag{7}$$

where $\boldsymbol{\epsilon}_r$ is the complex relative dielectric constant tensor. Using the standard procedure for FEM calculations [62], this equation is recast in a variational form by premultiplying with a "test" magnetic field $\widetilde{\mathbf{H}}$ and using the Gauss' divergence theorem. This yields the weighted residual form of the eigenvalue equation,

$$\int \int_{\Omega} [(\nabla \times \widetilde{\mathbf{H}}^*) \cdot \boldsymbol{\epsilon}_r^{-1} (\nabla \times \mathbf{H}) - \beta(\nabla \cdot \widetilde{\mathbf{H}}^*)(\nabla \cdot \mathbf{H})$$

$$- k_0^2 (\widetilde{\mathbf{H}}^* \cdot \mathbf{H})]dV = 0. \tag{8}$$

Here, Ω is the simulation domain and k_0 is the free-space wave vector of the resonant mode. The second term inside the integral is the "penalty" term and is added to suppress spurious solutions to the problem. The strength of this term is controlled by the numerical parameter β. A commercially available FEM solver was configured to solve this as an eigenvalue problem for k_0 [63]. The calculation searches for the first-order radial modes at a free-space wavelength around a wavelength of interest. For estimation of the radiation loss, the power must be allowed to escape the simulation
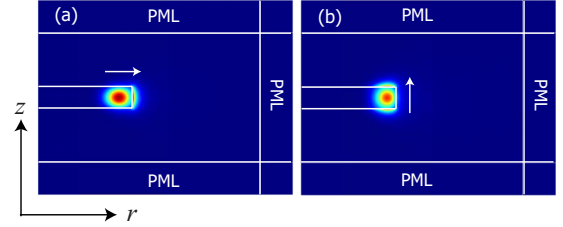

FIG. 3. (Color online) Magnitude of the electric field ($|\mathbf{E}|$) for the fundamental radial modes calculated by the full-vectorial FEM calculations. The dominant electric field components in (a) and (b) are, respectively, in the $\hat{r}$ and $\hat{z}$ directions and are indicated by arrows. The boundaries are truncated by cylindrical PMLs to allow for the power to escape the simulation domain.

domain which is achieved by terminating the boundary with cylindrical perfectly matched layers (PMLs). The PMLs must be placed at such a distance that the calculated radiation loss does not vary with the PML parameters and is thus indicative of the loss of the structure itself. The optimized PML parameters are taken from literature [62]. PML termination of the boundary yields a complex eigenvalue, k_0 and a corresponding radiation Q given by

$$Q_{rad} = \frac{\text{Re}(k_0)}{2\,\text{Im}(k_0)}. \tag{9}$$

In order to verify the trends predicted by the ray-optics picture and for optimization of the disk geometry, we investigated the trends in Q as a function of its diameter and thickness. The results of FEM calculations for a wavelength around 750 nm (core refractive index of 1.73) are displayed in Figs. 3 and 4. Figures 3(a) and 3(b) show the typical electric field profiles for modes with the fields predominantly in the $\hat{r}$ and $\hat{z}$ directions, respectively. The full-vectorial nature of simulation captures the field discontinuities, which are essential for correctly modeling the interaction of the modes with the interfaces. As we will show in Sec. VII, scattering of the electromagnetic energy by the nonideal disk periphery is the chief loss mechanism that limits the Q in our structure. Since this loss is proportional to the normalized electric power at the disk periphery [64], it is expected that the $\hat{r}$ and $\hat{z}$ modes shown in Fig. 3 will have a different Q.

Figures 4(a) and 4(b) show the predicted evolution of the Q with the microdisk diameter, D, and the thickness, h, for two cases of propagation loss. The loss coefficient for calculating the radiation Q was assumed to be $\alpha_T = 0$ cm^{-1} while that for obtaining a total Q was assumed to be $\alpha_T = 100$ cm^{-1}. Choice of the latter value is motivated by the typical values of propagation loss observed for devices fabricated in the nc-Si system [51]. The radiation-limited quality factor varies exponentially with the disk diameter. With the inclusion of propagation loss, the exponential increase in Q saturates to a more-or-less constant value. In accordance with the ray-optics model, the total Q thus shows radiation- and loss-limited regimes. For smaller diameters, Q is limited by the radiation out of the disk, whereas for larger diameters it is loss (attenuation) limited. From Fig. 4 it is seen that the exact onset of the loss-limited regime depends upon the
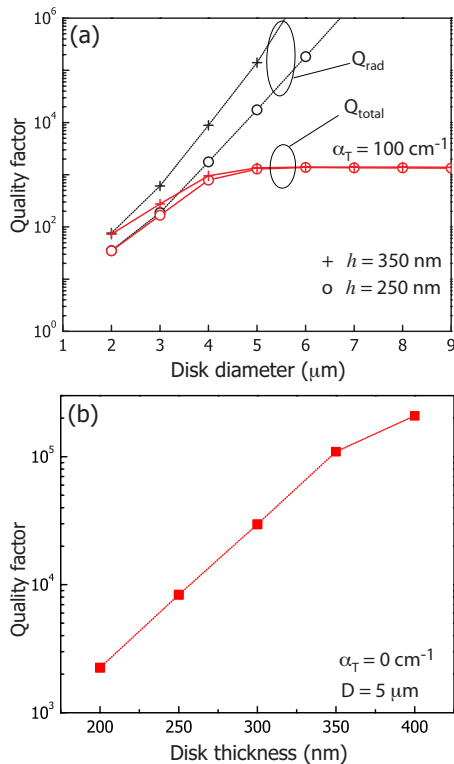
FIG. 4. (Color online) FEM calculated radiation and total quality factors as a function of disk dimensions in the vicinity of vacuum wavelength $\lambda \sim 750$ nm. Resonances of different sized disks occur at wavelengths slightly different from 750 nm. (a) The radiation Q (black, dotted curves) and total Q (red, solid curves) versus diameter for two different disk thicknesses indicated in the figure. (b) The variation of Q with h at a fixed diameter of 5 μm and $\alpha=0$ cm^{-1}.

propagation loss, α_T, and the disk thickness h (or, equivalently, the effective index). Figure 4(a) shows the size-dependent Q factor for two different disk thicknesses. To further illustrate the dependence of Q on disk thickness, we have plotted Q as a function of h (for a fixed $D=5$ μm) in Fig. 4(b) where Q is seen to depend exponentially on h.

In order to design structures with highest Q/V_m it is necessary to ensure that the Q is limited by the intrinsic propagation loss of the structure rather than by the radiation out of the disk. The numerical field calculations, such as presented in the present section, are therefore required for the design of microdisk resonator devices in low-index-contrast systems such as SRO air. The methodology developed here will also be used in Sec. VI to quantify the total loss observed in our fabricated structures.

V. FABRICATION AND TESTING OF MICRODISK RESONATORS

Using the simulations for the mode profile and quality factor from the preceding section as a first guess for the optimum structural dimensions, we fabricated pedestal supported SRO microdisk resonators containing silicon nanocrystals. Starting with unpatterned, annealed SRO films on Si
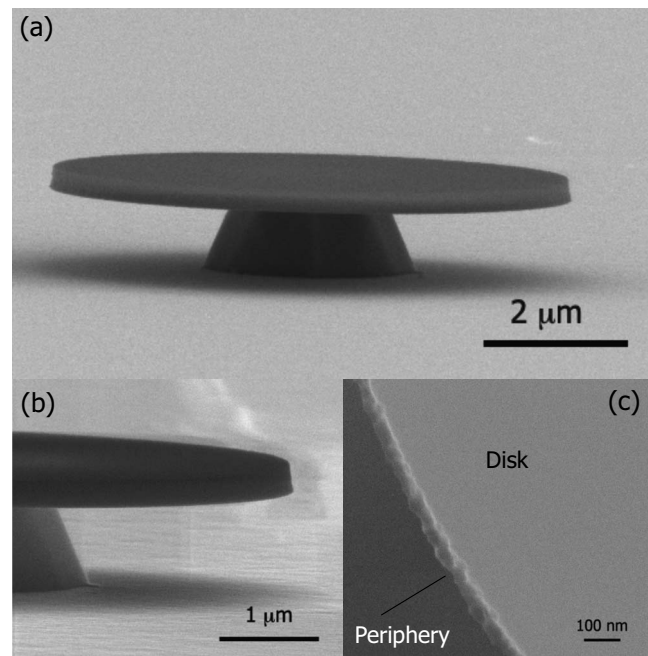

FIG. 5. Scanning electron micrographs of fabricated microdisk resonator devices. (a) The tilt angle view of the resonator showing the SRO disk and the Si pedestal on an Si substrate. (b) Close-up side view of the disk periphery showing the slightly tilted walls (c) High resolution top-view scanning electron microscopy image of the disk showing the line-edge roughness. The mean roughness estimated from this figure is $\sim 10-20$ nm.

substrates, circular areas with diameters varying between 2 μm-8 μm were defined using optical lithography. The silicon-rich oxide layer was subsequently dry-etched down to the underlying silicon substrate in NF$_3$ plasma using photoresist as a masking layer. Finally, silicon was undercut using tetramethylammonium hydroxide (TMAH) to form pedestals. The fabrication steps used here are fairly standard across many material systems [44,49–51,65–67].

Figure 5 shows scanning electron microscope images of typical finished devices. Figure 5(b) is a close-up view of the device sidewalls, which, in spite of dry etching, are slightly tilted. Figure 5(c) is a high-resolution top view of the disk periphery. Dry-etch-induced line-edge roughness (LER) is clearly visible on the sidewalls. The LER estimated from Fig. 5(c) is in the range of 10–20 nm. Quantitative statistical estimates of the root-mean-square (rms) LER require atomic force microscopy (AFM), the use of which is rendered difficult by the curvature of the device periphery. For curved resonators, there are recent examples where optical loss measurements themselves have been used for estimating LER parameters [64].

Accurate optical characterization of microdisk resonator devices requires collection of WGM PL of silicon nanocrystals with a high signal-to-background ratio. Several methods for collecting the WGM PL are reported in literature [44,65,68], each having tradeoffs in terms of the ease of implementation and the signal-to-background ratio. We have opted for free-space collection optics since it allows for collection of most of the modes excited in the cavity. As de-
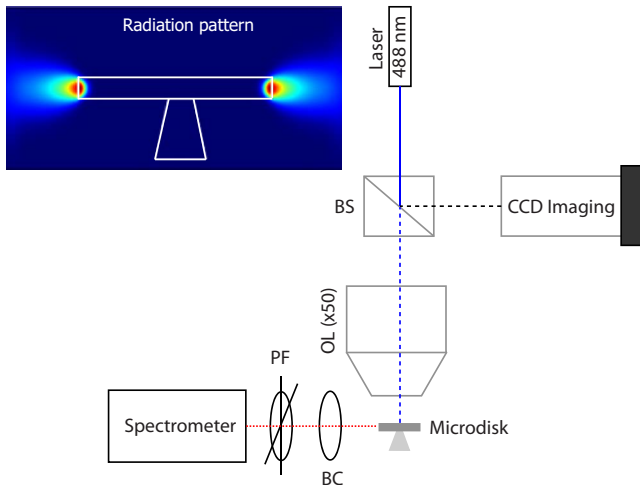
FIG. 6. (Color online) The optical setup used for collection of the WGM photoluminescence from the microdisk resonators. The Ar$^+$-ion excitation source is incident through a 50:50 beam splitter (BS) and a 50× objective lens (OL). The rapidly divergent WGM signal is collimated by a beam condenser (BC) lens assembly and passed into a spectrometer through a polarization filter (PF). The top-pump side-collection geometry is motivated by the radiation pattern (radial Poynting vector) of the microdisk mode shown in the inset.
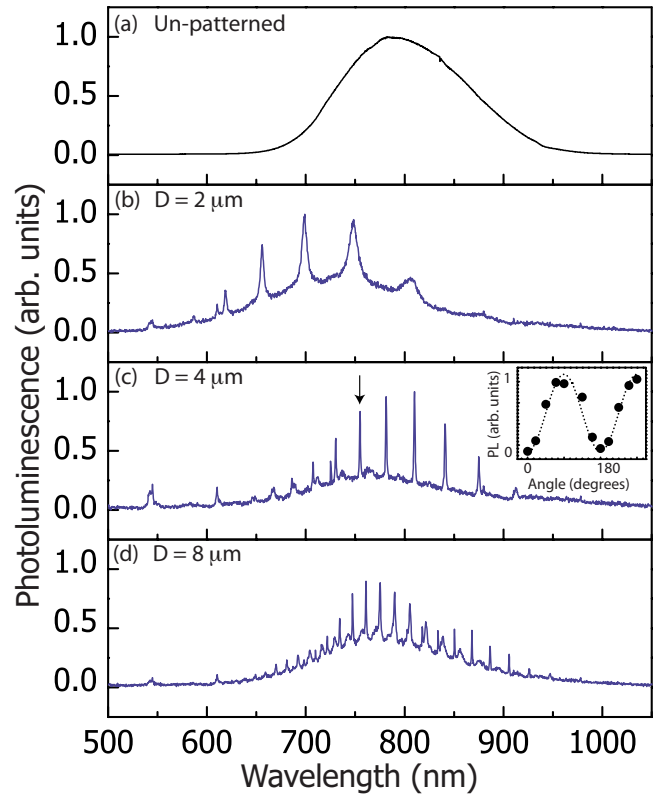

FIG. 7. (Color online) The typical WGM PL spectra of silicon nanocrystals in microdisks of various sizes. The spectra (blue lines) shown correspond to disk diameters of (b) 2 μm, (c) 4 μm, and (d) 8 μm. The black curve in (a) is the PL of an unpatterned SRO film and is shown for comparison. The inset in (c) shows the measured polarization dependence of the 750 nm peak (indicated by arrow) of a 4 μm disk (points) and the expected sinusoidal fit (dotted line) [69].

picted in the schematic of Fig. 6, the microdisk resonators are top excited by the 488 nm line of an Ar$^+$-ion laser through a 50× microscope objective having a numerical aperture of 0.55. The excitation power and spot size were approximately 1 μW and 1 μm resulting in an excitation intensity of about 130 W/cm^2. The WGM PL is collected by a lens assembly placed at right angles to the excitation optics. The choice of the orthogonal orientation of the collection optics is based on the FEM-calculated radiation pattern of the microdisk WGM shown in the inset. The collected WGM light passes through a polarization filter which allows a selective measurement of $\hat{r}$ and $\hat{z}$ polarized modes (Fig. 3). The PL is finally analyzed by a liquid nitrogen cooled imaging spectrometer with a spectral resolution of 0.07 nm.

VI. QUALITY FACTORS OF MICRODISKS CONTAINING Si NANOCRYSTALS

Figure 7 shows typical WGM PL spectra of microdisks and their comparison with the PL of an unpatterned nc-Si film. For the sake of clarity, only the spectra for 2 μm, 4 μm, and 8 μm disks are shown. The spectra show all the features expected from polarized cavity PL: (1) The broad nc-Si PL is modified to a series of sharp resonant peaks, (2) the free spectral range (which corresponds to the effective disk diameter) decreases monotonically with increasing diameter, and (3) the PL from the cavity shows specific polarizations [shown by the inset in Fig. 7(c)]. For a 2 μm diameter disk, resonant modes supported at wavelengths >750 nm are not well confined. These broad resonances are difficult to resolve over the background PL. Moreover, the WGMs emission has an angular dependence and the strength

of a particular WGM in the observed spectrum depends upon the position of the collection optics with respect to the microdisk. These factors lead to an apparent shift of the WGM spectrum relative to the PL of an unpatterned film.

Quality factors of resonator structures are generally wavelength dependent. For a fair comparison, the Q of disks with different diameters should therefore be measured at roughly the same wavelength. Because of a good signal-to-background ratio, here we focus on resonances of the structures in the vicinity of a free-space wavelength of ~750 nm. The Q of the structures as a function of disk diameter are plotted in Fig. 8. In order to find the total propagation loss of the structure, we focus on the resonance of a disk with diameter outside the radiation-limited regime. The total propagation loss α_T inside such a disk is obtained from its Q by use of Eq. (4). For our experiments, we obtain $\alpha_T = 120 \pm 10$ cm^{-1}.

Having obtained the propagation loss from the resonance width (FWHM) of any one structure, it is possible to calculate (numerically and with ray optics) the theoretical quality factors of the microdisk resonators for all the fabricated sizes. Using $\alpha_T = 120$ cm^{-1} in the FEM simulations, we can theoretically reproduce the entire curve for the size dependence of the quality factor obtained in our experiments. The
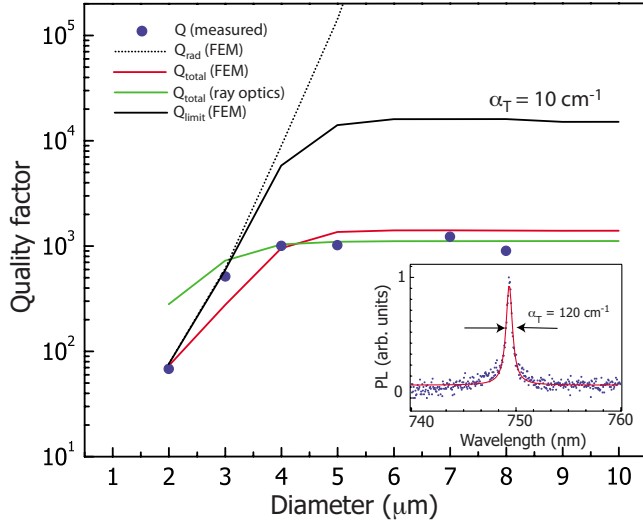
FIG. 8. (Color online) Q versus diameter from ray optics, FEM, and their comparison with measurement. The inset shows the measured 750 nm resonance of a 5 μm disk (blue dots). A Lorentzian fit [69] to the measured data (red curve) yields a total intensity loss coefficient $\alpha_T = 120$ cm^{-1}. This value is used to generate the FEM and ray-optics curves. The black dotted curve is the FEM calculation of radiation Q. FEM prediction of a theoretical, smooth sidewall, low-loss structure is shown by the solid black curve and its Q is expected to be as high as 1.5×10^4, limited only by the intrinsic material losses.

disks across the entire range of fabricated diameters are thus limited by a similar value of α_T, indicating the uniformity of the fabrication process. Figure 8 also shows the Q versus D behavior predicted by the ray-optics model [Eq. (4)]. The ray-optics model correctly captures the loss-limited part of the Q versus D curve but overestimates the quality factor for disks with $D < 3$ μm. The radiation limited Q predicted by FEM calculations is plotted in the figure to show the boundary between radiation-limited and loss-limited Q's. For the SRO-air system used in the present work, the disks are observed to be radiation-limited for diameters of $D \lesssim 4$ μm. For later reference, Fig. 8 also shows the Q limited by the material loss (band-to-band absorption and the Mie scattering) of the embedded Si nanocrystals. This value represents the approximate maximum Q achievable in microdisk structures fully filled with nc-Si.

VII. ANALYSIS OF LOSS MECHANISMS IN SRO MICRODISK RESONATORS

The Q provides a measure of the total propagation loss in the system [Eq. (6)]. There are several factors which can contribute to this loss and understanding their significance in making up the total loss is necessary to analyze and improve the microdisk performance. Among the potentially dominant loss mechanisms are the radiation loss (α_{rad}), the band-to-band absorption (α_{BB}) and the volumetric scattering by the nanocrystals (α_{Mie}), the waveguide LER scattering loss (α_{LER}), and the free-carrier absorption loss (α_{FCA}).

$$\alpha_T = \alpha_{rad} + \alpha_{BB} + \alpha_{Mie} + \alpha_{LER} + \alpha_{FCA}. \quad (10)$$

In this section, we will analyze these loss mechanisms and, by looking at their wavelength dependence, identify the

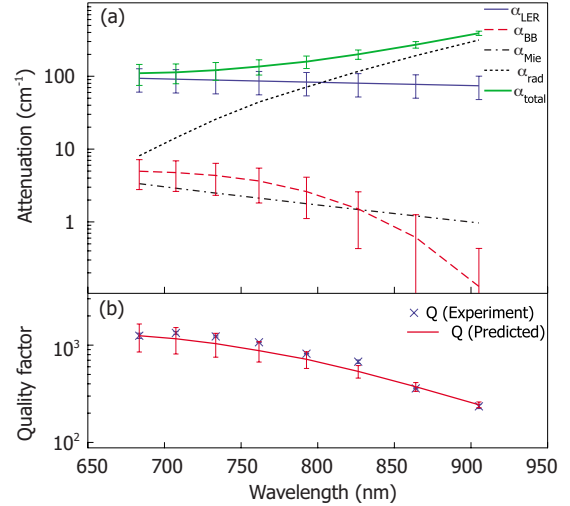FIG. 9. (Color online) (a) Wavelength dependence of the band-to-band absorption (α_{BB}), Mie scattering (α_{Mie}), LER scattering (α_{LER}), radiation loss (α_{rad}), and the total loss for a 4 μm diameter microdisk. (b) The Q based on the theoretical estimate of total loss in (a) and its comparison with experiment.

dominant sources of loss in various wavelength regimes in our experiments (see Fig. 9). Measurements and theoretical results presented in this section correspond to a 4 μm-diameter microdisk. The knowledge of the size distribution of nanocrystals is required in order to obtain accurate estimates for various loss mechanisms listed in Eq. (10). This is particularly important for loss mechanisms that are strongly nanocrystal size dependent. A direct determination of the number density of nanocrystals emitting at a given wavelength is difficult. This is because of difficulty associated with (1) correlating the observed size with emission wavelength and (2) ascribing a definite size to the observed crystalline region in an image [24]. The majority of studies, therefore, typically use the total density obtained from statistical analyses of TEM images [52]. Here we will use the nanocrystal size distribution, $\rho(R)$, obtained from the material excess of Si in our films by the procedure shown in the Appendix. This procedure appears to be in good agreement with TEM results from films synthesized under similar conditions [22,24].

A. Free-carrier absorption

The excited electrons and holes in the nanocrystals can absorb the light circulating in the WGM by free-carrier absorption [70]. For the optical system in our experiments, we begin to see the effect of free-carrier absorption for pump powers in excess of 1 mW [71]. For the measurements of Q presented in the preceding section, the excitation powers were kept well below 1 mW. α_{FCA} is thus not a significant contributor to the total loss.

B. Radiation loss

The radiation loss as a function of wavelength is obtained from the FEM calculations of the WGMs as shown in Sec.

IV. At a vacuum wavelength λ, the radiation Q is related to the radiation loss α_{rad} as

$$\alpha_{\text{rad}}(\lambda) = \frac{2\pi n_{\text{eff}}(\lambda)}{\lambda Q_{\text{rad}}(\lambda)}. \tag{11}$$

Here, $n_{\text{eff}}(\lambda)$ is the effective index of the slab waveguide mode obtained at wavelength λ. α_{rad} as a function of wavelength is plotted in Fig. 9(a) and it is seen to increase exponentially with the wavelength. For this particular case of a 4 μm diameter disk, radiation is the chief loss mechanism for wavelengths $\lambda > 800$ nm.

C. Band-to-band absorption in nanocrystals

The absorption of nc-Si thin films at wavelengths >700 nm is not strong enough to be measured by ellipsometry [56], whereas the accuracy of the Swanepoel method is limited to samples exhibiting loss >100 cm^{-1} [55]. Moreover, these measurements cannot distinguish between the band-to-band absorption and Mie scattering from nanocrystals. A first-order estimate of band-to-band absorption can be obtained with the knowledge of the absorption cross section, the nanocrystal size distribution, and the confinement factor, $\Gamma(\lambda)$, of the optical mode inside the disk (determined from FEM calculations).

In determining α_{BB}, it is to be noted that the total absorption at a wavelength λ comprises of absorption by all the nanocrystals with band gaps, $E_g \leq hc/\lambda$. If $\sigma_{\text{abs}}(\lambda)$ is the absorption cross section of the particle having an emission wavelength λ, then the total absorption is given by

$$\alpha_{\text{BB}}(\lambda) = \Gamma(\lambda) \int_{R=R(\lambda)}^{R=R_{\text{max}}} \sigma_{\text{abs}}(R)\rho(R)dR, \tag{12}$$

where $R(\lambda)$ is the radius of the nanocrystal with an emission wavelength λ. σ_{abs} is written as a function of R since it is related to the nanocrystal's emission wavelength [Eq. (A4)]. R_{max} is the radius of the largest nanocrystal in the ensemble and is obtained from the longest wavelength in the PL spectrum. In calculating α_{BB}, we have used typical numbers for the absorption cross sections reported in the literature [52]. α_{BB} obtained from Eq. (12) is shown in Fig. 9(a). It is seen that in the wavelength range probed in our experiments, α_{BB} is one of the less important losses in our devices.

D. Mie scattering by nanocrystals

Light scattering by particles is described by the Mie theory. In the limit where the particle dimensions are much smaller than the incident optical wavelength, the scattering cross section, σ_{Mie}, of a spherical nanocrystal of radius R at a vacuum wavelength λ is given by the Rayleigh formula [72]

$$\sigma_{\text{Mie}}(R,\lambda) = \frac{8\pi}{3}\left(\frac{2\pi n_{\text{SiO}_2}}{\lambda}\right)^4 R^6 \left(\frac{\epsilon_{\text{Si}} - \epsilon_{\text{SiO}_2}}{\epsilon_{\text{Si}} + 2\epsilon_{\text{SiO}_2}}\right)^2. \tag{13}$$

Here, $n_{\text{SiO}_2} = 1.46$ is the refractive index of the surrounding silica matrix, and ϵ_{Si} and ϵ_{SiO_2} are, respectively, the relative permittivities of the nanocrystal and the host matrix. Because

of a rather strong dependence on R, consideration of the size distribution is especially important in the estimation of the Mie scattering. Analogous to Eq. (12), we obtain the total Mie scattering at a wavelength λ by summing over the nanocrystal distribution

$$\alpha_{\text{Mie}}(\lambda) = \Gamma(\lambda) \int_{R=R_{\text{min}}}^{R=R_{\text{max}}} \sigma_{\text{Mie}}(R,\lambda)\rho(R)dR. \tag{14}$$

Evaluation of α_{Mie} is plotted in Fig. 9(a). Even with the ensemble effects included, Mie scattering is seen to be not very significant in the wavelength range in our experiments. We note that a related procedure has been recently used for obtaining total scattering loss due to nc-Si ensemble coated on microsphere resonators [73]. There, the scattering loss was estimated by assuming a Gaussian distribution of nanocrystal diameters and the effect of the distribution width was investigated. In our calculations, we have obtained the nanocrystal distribution directly from the spectral shape of our measured PL signal.

E. Line-edge roughness scattering

The microscopic local deviations of the disk periphery from perfect circularity cause light scattering and couple the energy in the WGMs to radiation modes. The resultant propagation loss is given by [74]

$$\alpha_{\text{LER}}(\lambda) = \frac{\xi^2 k_0^3}{2\sqrt{2}n_1(\lambda)}\{[n_1(\lambda)]^2 - 1\}$$
$$\times \frac{\{[n_1(\lambda)]^2 - [n_{\text{eff}}(\lambda)]^2\}}{1 + k_0 w\{[n_{\text{eff}}(\lambda)]^2 - 1\}^{1/2}}, \tag{15}$$

where $k_0 = 2\pi/\lambda$ is the vacuum wave vector, $n_1(\lambda)$ and $n_{\text{eff}}(\lambda)$ are, respectively, the refractive index and the effective index of the SRO film, ξ is the root-mean-square roughness of the waveguide, and w is the waveguide width. For a WGM, the effective waveguide width must be obtained from the mode profile calculation such as shown in Fig. 3. The index $n_1(\lambda)$ is known from the ellipsometric measurements (Sec. II) and $n_{\text{eff}}(\lambda)$ is obtained from the solution of the slab waveguide equation. ξ is estimated from the SEM image to be 17 ± 3 nm. Figure 9(a) shows the result of evaluation of Eq. (15). α_{LER} is seen to be the main contributor to the total loss for wavelengths below 800 nm. More accurate evaluation of α_{LER} will require statistical information about the roughness (correlation length, rms value of ξ) and must be obtained by techniques such as AFM which was not performed for the present work.

Figure 9(a) also shows the total loss obtained by summing the various contributions estimated in the preceding sections. The resultant Q corresponding to the estimated total loss is plotted in Fig. 9(b). Within the approximations used for estimating the various loss contributions, there is a good agreement between the experimental and theoretical values of the total Q. Figure 9(a) indicates that at wavelengths below 800 nm, the LER scattering is the dominant loss mechanism in our resonators. Because of the ξ^2 dependence of α_{LER} on roughness, efforts to improve the quality factors of microdisk

resonators in the SRO system will need to identify etching procedures which yield smoother disk peripheries.

VIII. PROSPECT FOR PURCELL EFFECT AND LASING IN Si QDS

Semiconductor QDs placed in microdisk cavities undergo a change in their emission characteristics. In addition to being useful for various devices, such changes can be used to probe the unknown properties of the emitting quantum dots. In particular, a change in spontaneous emission lifetime can be used to gain understanding of the luminescence efficiency of the QD ensemble [75]. Temperature-dependent measurement of this emission efficiency can potentially shed light on the phonon-assisted processes and the line broadening mechanisms in nc-Si [28]. Here, we evaluate the magnitude of the maximum possible radiative-rate enhancement in our microdisk structures based on the experimental quality factors achieved and the calculated modal volumes. For an emitter with a linewidth much smaller than the cavity resonance width, the enhancement of the spontaneous emission rate in the cavity (Γ_c^{rad}) over that in an unpatterned medium of the same refractive index (Γ_0^{rad}) is defined as the Purcell factor, F_P, and is given by [76]

$$F_P = \frac{\Gamma_c^{rad}}{\Gamma_0^{rad}} = \frac{3}{4\pi^2}\frac{Q}{\widetilde{V}_m}\eta. \qquad (16)$$

Here, $\widetilde{V}_m$ is the normalized modal volume (i.e., measured in the units of cubic wavelengths in the material of refractive index n)

$$\widetilde{V}_m = \frac{1}{(\lambda/n)^3}\frac{\int_V \epsilon_r(\mathbf{r})|\mathbf{E}(\mathbf{r})|^2 dV}{\max[\epsilon_r(\mathbf{r})|\mathbf{E}(\mathbf{r})|^2]}, \qquad (17)$$

and η is a factor which measures the spatial and spectral misalignment of the quantum dot with respect to the resonant electric field inside the cavity. In the absence of any misalignments (η=1), Eq. (16) represents the maximum Purcell enhancement possible for a given cavity. We stress that Eq. (16) gives the Purcell factor of a cavity-QD system having a QD linewidth≪cavity linewidth. For most cavity-QD systems, this is true only at low (<10 K) temperatures. The maximum Purcell factors evaluated in this section are obtained under the assumption that the nc-Si-doped microdisks are operating at low temperatures. Figure 10 plots the maximum achievable, low-temperature Purcell factors using our experimentally obtained quality factors and modal volumes computed from FEM. The theoretical maximum Purcell factor possible in our structures is approximately 6. The observed enhancement depends not only upon Q/V_m but also upon the linewidth, orientation, and placement of the QD inside the cavity and is typically less than the predicted maximum. As stated earlier, the Q/V_m in our experiments is limited by the LER scattering loss which is proportional to the square of roughness (ξ^2). Reducing ξ from ~20 nm to ~5 nm will make the LER scattering loss α_{LER} less than the intrinsic loss of the structure ($\alpha_{BB}+\alpha_{Mie}$). It is thus possible to increase the Q/V_m by an order of magnitude making the
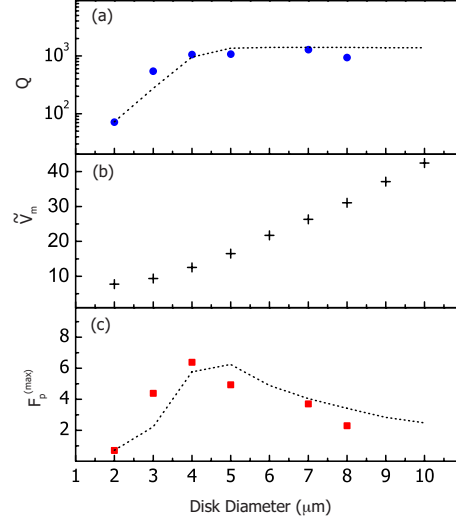

FIG. 10. (Color online) (a) Quality factor, (b) mode volume, and (c) maximum achievable Purcell factors for our fabricated microdisk resonators. The dotted lines in (a) and (c) represent the values predicted by FEM calculations and the data points are the values predicted from experimental quality factors.

maximum spontaneous emission rate enhancement of the order of 50.

Achieving a net optical gain in the nc-Si system has been challenging and typical studies have been able to reproducibly observe gain only under pulsed excitation [29–31]. The magnitude and duration of the gain is limited by Auger recombination (AR) of the excited carriers, which occurs with a characteristic time scale of approximately nanoseconds. The radiative lifetimes in nc-Si on the order of tens of μs make it a formidable challenge to overcome AR. In comparison, the radiative lifetimes in III-V systems are hundreds of picoseconds which enable a strong inversion of these gain media without significant AR. Owing to this stiff competition between radiative processes and AR in nc-Si, cavity induced enhancement in the spontaneous and stimulated emission of nc-Si is likely to have important implications in the eventual balance between the radiative and nonradiative processes.

IX. CONCLUSIONS

We have presented a detailed analytical, numerical and experimental study of microdisk resonators containing silicon quantum dots emitting in the visible-NIR wavelength range. By deriving a simple analytical expression for the size dependence of the quality factors, we have identified two regimes of the microdisk resonator operation, which are not usually considered significant in similar structures fabricated in high-index-contrast systems. Optimization of realistic disk structures with respect to their dimensions was achieved by FEM calculations of the whispering gallery modes. These calculations confirmed the two size-dependent regimes predicted by ray optics and also highlighted its range of applicability.

We have fabricated nc-Si-containing microdisk resonators with diameters down to 2 μm and demonstrated cavity Q

$>10^3$ at 750 nm wavelength for microdisks with diameters ≥ 4 μm. The highest value of Q/V_m is obtained at $D = 4$ μm, where the radiation and propagation losses are equal. At a wavelength of 750 nm, the total propagation loss for our structures across the entire range of sizes is found to be $\sim$120 cm^{-1}. This number is explained by analyzing the contribution of five different possible loss mechanisms to the total propagation loss. This analysis included the effects of nanocrystal size distribution to account for the strong size dependence of some of the optical loss processes. It is seen that the total loss is dominated by different mechanisms in the two wavelength regimes. For the particular case of a 4 μm-diameter disk, we found that the Q is limited by the LER scattering for wavelengths ≤ 800 nm and by the radiation loss for wavelengths ≥ 800 nm.

The microdisk resonators in our work are predicted to work well for bringing about enhancement of spontaneous emission rate in silicon nanocrystals with a maximum predicted Purcell factor of $\sim$6. SRO is a relatively new material system and an optimization of etching process leading to a reduction of LER to about 5 nm should enable the realization of resonators limited only by the material absorption and Mie scattering of the embedded quantum dots. Our simulations predict the maximum achievable Q in this regime to be $>1.5 \times 10^4$ for disk diameters ≥ 5 μm at 750 nm wavelength. Realization of such Q in microdisk resonators can be expected to yield maximum low-temperature Purcell factors on the order of 50. The present work, therefore, has important implications from the points of view of fundamental studies as well as demonstration of visible wavelength lasing in silicon nanocrystals.

APPENDIX: DETERMINATION OF NANOCRYSTAL SIZE DISTRIBUTION $\rho(R)$

In the following, we will determine the nanocrystal size distribution with the knowledge of the PL spectrum and the excess Si concentration. The size distribution, $\rho(R)$, is defined as the number of nanocrystals per unit volume with radius between R and $R+dR$ and it is measured in units of cm^{-3} nm^{-1}.

Let us assume that the Si and O atomic-% in the films as determined by the Rutherford backscattering spectroscopy (RBS) are x_{Si} and x_O, respectively. Also, let V_{SiO_2} and V_{Si} be the respective volumes of the stoichiometric oxide and the clustered silicon phases. Since each SiO$_2$ molecule yields one Si and two O atoms, the result of the RBS measurement can be written as

$$\frac{\rho_{SiO_2}V_{SiO_2}/A_{SiO_2} + \rho_{Si}V_{Si}/A_{Si}}{3\rho_{SiO_2}V_{SiO_2}/A_{SiO_2} + \rho_{Si}V_{Si}/A_{Si}} = \frac{x_{Si}}{x_{Si}+x_O}. \quad \text{(A1)}$$

Here, $\rho_{Si}(\rho_{SiO_2}) = 2.33(2.2)$ g/cm^3 and $A_{Si}(A_{SiO_2}) = 28(60)$ amu are the density and the atomic mass of the silicon (stoichiometric oxide) phase, respectively.

The number density, N_{Si}, of the excess silicon atoms (present in the form of nanocrystals) is

$$N_{Si} = \frac{\rho_{Si}/A_{Si}}{1 + V_{SiO_2}/V_{Si}}. \quad \text{(A2)}$$

The volume ratio, V_{SiO_2}/V_{Si}, in Eq. (A2) is determined from Eq. (A1).

Now we assume that the nanocrystal size distribution $\rho(R)$ is proportional to the spectral shape of the normalized PL, $I_{PL}(R)$,

$$\rho(R) = AI_{PL}(R), \quad \text{(A3)}$$

where A is the proportionality constant to be determined. Equation (A3) is written as a function of the nanocrystal radius, R, which is related to its free-space emission wavelength λ according to [5]

$$\frac{hc}{\lambda} = E_{g,Si} + \frac{3.73}{(2R)^{1.39}}, \quad \text{(A4)}$$

where $E_{g,Si} = 1.12$ eV is the band gap of bulk silicon, and h and c are Planck's constant and the velocity of light, respectively. Inherent in Eq. (A3) is an implicit assumption that the PL quantum efficiency (QE) of nanocrystals is uniform across the entire size distribution. This assumption is supported by the recent reports on the measurement of QE of nc-Si, which show that it varies by $<10\%$ over the wavelength range from 700 nm to 850 nm [75]. If we assume that a complete separation between Si and SiO$_2$ phases occurs as a result of annealing at 1100 °C, the excess Si atoms are all distributed in nanoclusters. The total number of excess Si atoms per unit volume is obtained by finding the total integrated volume of the nanocrystals and dividing by the volume of 1 Si atom in a crystal (which is assumed to be $(\frac{1}{8})$th of the Si unit-cell volume). The proportionality constant A is then determined by equating this number with the number density of the excess Si atoms from the RBS measurement

$$N_{Si} = \int_{R=R_{min}}^{R=R_{max}} \frac{\frac{4}{3}\pi R^3}{\frac{1}{8}a^3}\rho(R)dR, \quad \text{(A5)}$$

where a is the lattice constant of Si. Equation (A2) assumes nanocrystals of a spherical shape. Although this is not strictly true for all the nanocrystals, the error resulting from non-sphericity is much less than the experimental error in the determination of stoichiometric composition of the films (few %). Using Eqs. (A2) and (A5) and $x_{Si} = 42\% \pm 2\%$ and $x_O = 48\% \pm 2\%$ as obtained in our experiment, we obtain $A = (1.5 \pm 0.1) \times 10^{25}$ cm^{-3} nm^{-1}. We can also find the total

nanocrystal number density N by integrating between the limits of the PL spectrum

$$N_{\text{QD}} = \int_{R=R_{\min}}^{R=R_{\max}} \rho(R)dR. \tag{A6}$$

For the value of A obtained above, we find $N_{\text{QD}} = (2.0 \pm 0.2) \times 10^{18}$ cm^{-3}. The RBS analysis also reveals that our films contain about 10% of nitrogen—a standard feature in nc-Si films prepared with PECVD of silane and nitrous oxide [22,24]. Because of this nitrogen content, we expect

about a 10% uncertainty in our determination of nanocrystal distribution. The above value of nanocrystal density is in good agreement with those obtained from TEM analyses of samples prepared under the same conditions [22,24].

It is possible that a fraction of the nanocrystal ensemble is optically inactive and is not represented in the PL spectrum. This fraction may still contribute to the loss mechanisms (in particular, the Mie scattering). However, since our estimate of nanocrystal density is based on the material excess of Si in the annealed SRO film, Eqs. (A2) and (A5) account for the optically dead fraction of the nanocrystal ensemble.

[1] L. Pavesi, L. Dal Negro, C. Mazzoleni, G. Franzò, and F. Priolo, Nature (London) **408**, 440 (2000).

[2] R. J. Walters, G. I. Bourianoff, and H. A. Atwater, Nat. Mater. **4**, 143 (2005).

[3] R. J. Walters, J. Carreras, T. Feng, L. D. Bell, and H. A. Atwater, IEEE J. Sel. Top. Quantum Electron. **12**, 1647 (2006).

[4] C. D. Presti *et al.*, Appl. Phys. Lett. **88**, 033501 (2006).

[5] C. Delerue, G. Allan, and M. Lannoo, Phys. Rev. B **48**, 11024 (1993).

[6] C. Delerue, M. Lannoo, G. Allan, E. Martin, I. Mihalcescu, J. C. Vial, R. Romestain, F. Muller, and A. Bsiesy, Phys. Rev. Lett. **75**, 2228 (1995).

[7] D. Kovalev H. Heckler, M. Ben-Chorin, G. Polisski, M. Schwartzkopff, and F. Koch, Phys. Rev. Lett. **81**, 2803 (1998).

[8] M. V. Wolkin, J. Jorne, P. M. Fauchet, G. Allan, and C. Delerue, Phys. Rev. Lett. **82**, 197 (1999).

[9] C. Delerue, M. Lannoo, and G. Allan, Phys. Rev. Lett. **84**, 2457 (2000).

[10] D. Kovalev, J. Diener, H. Heckler, G. Polisski, N. Kunzner, and F. Koch, Phys. Rev. B **61**, 4485 (2000).

[11] C. Delerue, G. Allan, and M. Lannoo, Phys. Rev. B **64**, 193402 (2001).

[12] G. Allan and C. Delerue, Phys. Rev. B **66**, 233303 (2002).

[13] D. Kovalev, E. Gross, N. Kunzner, F. Koch, V. Y. Timoshenko, and M. Fujii, Phys. Rev. Lett. **89**, 137401 (2002).

[14] C. Delerue, G. Allan, C. Reynaud, O. Guillois, G. Ledoux, and F. Huisken, Phys. Rev. B **73**, 235318 (2006).

[15] A. Guichard, D. Barsic, S. Sharma, T. Kamins, and M. Brongersma, Nano Lett. **6**, 2140 (2006).

[16] L. Tsybeskov, J. V. Vandyshev, and P. M. Fauchet, Phys. Rev. B **49**, 7821 (1994).

[17] M. Fujii, M. Yoshida, S. Hayashi, and K. Yamamoto, J. Appl. Phys. **84**, 4525 (1998).

[18] P. G. Kik, M. L. Brongersma, and A. Polman, Appl. Phys. Lett. **76**, 2325 (2000).

[19] I. Izeddin, A. S. Moskalenko, I. N. Yassievich, M. Fujii, and T. Gregorkiewicz, Phys. Rev. Lett. **97**, 207401 (2006).

[20] T. Nakamura, M. Fujii, S. Miura, M. Inui, and S. Hayashi, Phys. Rev. B **74**, 045302 (2006).

[21] O. Savchyn, F. R. Ruhge, P. G. Kik, R. M. Todi, K. R. Coffey, H. Nukala, and H. Heinrich, Phys. Rev. B **76**, 195419 (2007).

[22] F. Iacona, G. Franzò, and C. Spinella, J. Appl. Phys. **87**, 1295 (2000).

[23] V. Vinciguerra, G. Franzò, F. Priolo, F. Iacona, and C. Spinella,

[—] J. Appl. Phys. **87**, 8165 (2000).

[24] F. Iacona, C. Bongiorno, C. Spinella, S. Boninelli, and F. Priolo, J. Appl. Phys. **95**, 3723 (2004).

[25] N. Daldosso *et al.*, J. Appl. Phys. **101**, 113510 (2007).

[26] J. Diener, M. Ben-Chorin, D. I. Kovalev, S. D. Ganichev, and F. Koch, Phys. Rev. B **52**, R8617 (1995).

[27] I. Sychugov, R. Juhasz, J. Linnros, and J. Valenta, Phys. Rev. B **71**, 115331 (2005).

[28] I. Sychugov, R. Juhasz, J. Valenta, and J. Linnros, Phys. Rev. Lett. **94**, 087405 (2005).

[29] L. Khriachtchev, M. Räsänen, S. Novikov, and J. Sinkkonen, Appl. Phys. Lett. **79**, 1249 (2001).

[30] L. D. Negro *et al.*, Appl. Phys. Lett. **82**, 4636 (2003).

[31] P. M. Fauchet *et al.*, Opt. Mater. (Amsterdam, Neth.) **27**, 745 (2005).

[32] T. Baba, IEEE J. Sel. Top. Quantum Electron. **3**, 808 (1997).

[33] K. J. Vahala, Nature (London) **424**, 839 (2003).

[34] J. Vučković, M. Lončar, H. Mabuchi, and A. Scherer, Phys. Rev. E **65**, 016608 (2001).

[35] J. Vučković, M. Pelton, A. Scherer, and Y. Yamamoto, Phys. Rev. A **66**, 023808 (2002).

[36] J. R. Buck and H. J. Kimble, Phys. Rev. A **67**, 033806 (2003).

[37] S. M. Spillane, T. J. Kippenberg, K. J. Vahala, K. W. Goh, E. Wilcut, and H. J. Kimble, Phys. Rev. A **71**, 013817 (2005).

[38] V. Sandoghdar, F. Treussart, J. Hare, V. Lefevre-Seguin, J. M. Raimond, and S. Haroche, Phys. Rev. A **54**, R1777 (1996).

[39] D. W. Vernooy, A. Furusawa, N. P. Georgiades, V. S. Ilchenko, and H. J. Kimble, Phys. Rev. A **57**, R2293 (1998).

[40] Y. Xu, R. K. Lee, and A. Yariv, Phys. Rev. A **61**, 033808 (2000).

[41] T. A. Brun and H. Wang, Phys. Rev. A **61**, 032307 (2000).

[42] M. Rosenblit, P. Horak, S. Helsby, and R. Folman, Phys. Rev. A **70**, 053808 (2004).

[43] Y. Louyer, D. Meschede, and A. Rauschenbeutel, Phys. Rev. A **72**, 031801(R) (2005).

[44] K. Srinivasan, A. Stintz, S. Krishna, and O. Painter, Phys. Rev. B **72**, 205318 (2005).

[45] J. Wiersig and M. Hentschel, Phys. Rev. A **73**, 031802(R) (2006).

[46] T. J. Kippenberg, J. Kalkman, A. Polman, and K. J. Vahala, Phys. Rev. A **74**, 051802(R) (2006).

[47] J.-W. Ryu, S.-Y. Lee, C.-M. Kim, and Y.-J. Park, Phys. Rev. A **74**, 013804 (2006).

[48] Y.-D. Yang, Y.-Z. Huang, and Q. Chen, Phys. Rev. A **75**,

013817 (2007).

[49] K. Srinivasan and O. Painter, Phys. Rev. A **75**, 023814 (2007).

[50] M. Borselli, T. Johnson, and O. Painter, Opt. Express **13**, 1515 (2005).

[51] R.-J. Zhang, S.-Y. Seo, A. P. Milenin, M. Zacharias, and U. Gösele, Appl. Phys. Lett. **88**, 153120 (2006).

[52] N. Daldosso *et al.*, J. Lumin. **121**, 344 (2006).

[53] A. Tewary, R. D. Kekatpure, and M. L. Brongersma, Appl. Phys. Lett. **88**, 093114 (2006).

[54] A. Tewary, Ph.D. thesis, Stanford University, 2006.

[55] R. Swanepoel, J. Phys. E **16**, 1214 (1983).

[56] D. Amans *et al.*, J. Appl. Phys. **93**, 4173 (2003).

[57] S. L. McCall, A. F. J. Levi, R. E. Slusher, S. J. Pearton, and R. A. Logan, Appl. Phys. Lett. **60**, 289 (1992).

[58] S. C. Hagness, D. Rafizadeh, S. T. Ho, and A. Taflove, J. Lightwave Technol. **15**, 2154 (1997).

[59] N. C. Frateschi and A. F. J. Levi, J. Appl. Phys. **80**, 644 (1996).

[60] C. R. Pollock, *Fundamentals of Optoelectronics* (McGraw-Hill, New York, 2003).

[61] M. Oxborrow, IEEE Trans. Microwave Theory Tech. **55**, 1209 (2007).

[62] J. Jin, *The Finite Element Method in Electromagnetics*, 2nd ed. (Wiley, New York, 2002).

[63] Comsol multiphysics v. 3.3a (http://www.comsol.com), 2007.

[64] V. Van, P. P. Absil, J. V. Hryniewicz, and P.-T. Ho, J. Lightwave Technol. **19**, 1734 (2001).

[65] B. Gayral *et al.*, Appl. Phys. Lett. **75**, 1908 (1999).

[66] B. Gayral, J.-M. Gérard, B. Sermage, A. Lemaître, and C. Dupuis, Appl. Phys. Lett. **78**, 2828 (2001).

[67] X. Liu *et al.*, Appl. Phys. Lett. **84**, 2488 (2004).

[68] P. Michler *et al.*, Science **290**, 2282 (2000).

[69] E. Hecht, *Optics*, 2nd ed. (Addison-Wesley, New York, 1987), pp. 326 and 412.

[70] D. K. Schroder, R. N. Thomas, and J. C. Swartz, IEEE J. Solid-State Circuits **13**, 180 (1978).

[71] R. D. Kekatpure and M. L. Brongersma (unpublished).

[72] A. J. Cox, A. J. DeWeerd, and J. Linden, Am. J. Phys. **70**, 620 (2002).

[73] J.-Y. Sung, A. Tewary, M. L. Brongersma, and J. H. Shin, IEEE J. Sel. Top. Quantum Electron. **12**, 1388 (2006).

[74] F. P. Payne and J. P. R. Lacey, Opt. Quantum Electron. **26**, 977 (1994).

[75] R. J. Walters, J. Kalkman, A. Polman, H. A. Atwater, and M. J. A. de Dood, Phys. Rev. B **73**, 132302 (2006).

[76] J. M. Gérard and B. Gayral, J. Lightwave Technol. **17**, 2089 (1999).